

# Deterministic single-soliton Kerr comb generation in a microring resonator by seeding with a pulsed trigger

Zhe Kang<sup>1,†</sup>, Jinhui Yuan<sup>1,2,\*†</sup>, Feng Li<sup>1,3,\*†</sup>, K. Nakkeeran<sup>4</sup>, J. Nathan Kutz<sup>5</sup>, Xianting Zhang<sup>1</sup>, Chao Mei<sup>2</sup>, Xinzhu Sang<sup>2</sup>, Qiang Wu<sup>6</sup>, Xian Zhou<sup>1</sup>, Chongxiu Yu<sup>2</sup>, Chao Lu<sup>1</sup>, Hwa Yaw Tam<sup>7</sup>, and P. K. A. Wai<sup>1,3</sup>

<sup>1</sup>Photonics Research Centre, Department of Electronic and Information Engineering, The Hong Kong Polytechnic University, Hung Hom, Kowloon, Hong Kong.

<sup>2</sup>State Key Laboratory of Information Photonics and Optical Communications, Beijing University of Posts and Telecommunications, 100876, Beijing, China.

<sup>3</sup>The Hong Kong Polytechnic University Shenzhen Research Institute, Shenzhen, 518057, Shenzhen, China.

<sup>4</sup>School of Engineering, University of Aberdeen, Aberdeen, AB24 3UE, United Kingdom.

<sup>5</sup>Department of Mathematics, University of Washington, Seattle, WA 98195, United States.

<sup>6</sup>Department of Physics and Electrical Engineering, Northumbria University, Newcastle upon Tyne, NE1 8ST, United Kingdom.

<sup>7</sup>Photonics Research Centre, Department of Electrical Engineering, The Hong Kong Polytechnic University, Hung Hom, Kowloon, Hong Kong.

## Corresponding author

\*yuanjinhui81@163.com, lifeng.hk@gmail.com.

**ABSTRACT:** Single-soliton Kerr frequency comb generation and maintenance in monolithic microresonators recently attracts great interests because it is the key to enable chip-scale optical frequency combs, optical synthesis of ultrashort pulses, coherent communication systems, etc. It however remains challenging to straightforwardly and deterministically achieve and maintain the attractive single-soliton state in microresonators. In this paper, for the first time, we propose and comprehensively demonstrate to excite the single-soliton Kerr comb in anomalous dispersion regime of Si<sub>3</sub>N<sub>4</sub> microring resonators by seeding the continuous-wave pump field with a pulsed trigger. We show that with sufficient single pulse energy, a pulse train with low repetition rate and even a single pulse trigger can both generate Kerr comb with deterministic single-soliton state without experiencing any unstable or chaotic states. Neither the pump frequency nor the cavity resonance is required to be actively tuned in the whole process, which are the common approaches reported so far. The mode-locked single-soliton Kerr comb generated is robust and insensitive to noise perturbations. The use of single pulse trigger makes it possible to manipulate the number and temporal locations of cavity solitons inside the cavity by controlling the power and temporal location of the trigger pulse. The proposed single pulse trigger approach is confirmed to be valid when the thermal dynamics of the cavity is included into the model. The excited cavity soliton can survive and be self-stabilized under the thermal perturbation to the resonant frequency of the Si<sub>3</sub>N<sub>4</sub> microresonator that raising from the absorption of the intracavity power.

**KEYWORDS:** Kerr frequency comb, cavity soliton, microresonator, deterministic, thermal dynamics.

## 1. INTRODUCTION

Since the self-referencing technique for carrier-envelope phase (CEP) stabilization was proposed in 2000 [1], optical frequency combs lead to revolutionary breakthrough in many fields such as spectroscopy, metrology, communications, biochemical sensing, and etc [2-4]. Kerr frequency combs, as a branch of the frequency comb family, can be formed through modulation instability (MI) and

cascaded four-wave mixing (FWM) in externally driven nonlinear microresonators [5-7]. Microresonators, typically structured as disks [5,8], toroids [9,10], or rings [11,12], have the advantages of compactness, high finesse, and CMOS compatibility. Externally driven microresonators are intrinsically driven-damped nonlinear systems, which normally exhibit multistable and chaotic dynamics depending on the system parameters [13]. Such dynamics have been observed in experiments of microresonator-based Kerr frequency comb formation in 2014 [14]. Temporal dissipative solitons, which are stable solitons superimposed on a continuous-wave (CW) background, can be achieved through comb formation. Especially, the single cavity soliton (SCS) state shows many attractive characteristics, e.g. generation of few-cycle femtosecond pulses at THz repetition rate and octave spanning phase-locked comb spectra [14-17]. It however remains challenging to straightforwardly and deterministically obtain the desired single-soliton state. The typical approach to obtain the single-soliton Kerr combs is to tune the pump frequency across the resonant frequency of the cavity, so that the effective red-detuned pumping condition is satisfied [14-20]. Various improvements to the basic pump tuning scheme have been proposed. They include the combined forward and backward pump tuning to successively reduce the number of solitons generated in the microresonator [21,22], a two-step “power kicking” protocol to overcome the impact of thermal destabilization [23,24], and a specified tuning pathway obtained by prior scanning of the parameters space to obtain deterministic SCS by avoiding the chaotic and unstable states [25]. However, tunable lasers generally suffer from broad linewidth and thus high noise density, which degrades the comb stability. Tuning the cavity resonance by current-controlled resistive heater has been proposed to excite single-soliton with frequency-fixed pump lasers [26]. Recent works showed that electrically adjusting the free-carrier lifetime of silicon microresonator can also lead to single-soliton mode-locking with a fixed pump frequency [27]. Although these tuning based approaches show promising performances, it would be more attractive to straightforwardly and deterministically generate the SCS state without any active control. Phase modulation of the pump field has been proposed to excite SCS instead of tuning the pump frequency [28-32]. However, the roundtrip times of compact microresonators are typically only few picoseconds. Currently there are no commercial available phase modulators that could satisfy such high-speed operation.

In this paper, we propose to straightforwardly generate the single-soliton Kerr comb by seeding the CW pumped cavity with a pulsed trigger. The CW pump frequency and the detuning between the pump and the cold cavity resonant frequency are fixed without any tuning process. Although similar cavity soliton excitation schemes by using addressing pulse were proposed in spatial structures [33,34] and fiber cavities [35-37] for optical memory and trapping applications, to the best of our knowledge, such triggering scheme was not reported for Kerr comb generation in ultra-compact (typically several pico-seconds per roundtrip) microresonators. In microresonators, the ultrashort roundtrip time is typically comparable to or even shorter than the duration of the trigger pulse, thus the trials of the full trigger pulse will be leaked into adjacent multiple roundtrips of the cavity. The coherent stacking of the pulse trials at each roundtrip may cause destructive perturbation to the intracavity field. On the other hand, the intrinsic strong thermal effects owing to the small volume and high absorption of microresonators will induce frequency shift of the cavity resonance to destabilize the cavity solitons. Both of the above problems do not exist in large volume fiber and spatial cavities and therefore make the proposed trigger approach in microresonators quite unique. The performance of the proposed trigger approach is numerically studied and discussed based on anomalous dispersive silicon nitride ( $\text{Si}_3\text{N}_4$ ) microring resonators.

## 2. PRINCIPLE

Figure 1(a) demonstrates the proposed scheme of the Kerr comb formation. An  $\text{Si}_3\text{N}_4$  microring resonator fabricated on silicon oxide substrate is used as the nonlinear cavity, which is similar to that in Ref. [12,18]. The resonator has a free spectral range (FSR) of 226 GHz, corresponding to a roundtrip time  $t_R = 4.425$  ps. The radius of the microring is  $r = 100$   $\mu\text{m}$  and the coupling coefficient between the bus and ring waveguides is  $\theta = 0.25\%$ . The loaded Q-factor is  $\sim 1 \times 10^5$ . The width and height of the waveguide cross-section are 1650 and 730 nm, respectively. Figure 1(b) shows the group velocity dispersion (GVD) of the quasi-TE mode versus wavelength calculated with the full-vector finite element method. The dispersion coefficient at 1550 nm is 46.3 ps/nm.km. The inset of Figure 1(b) shows the electric field distribution of the quasi-TE mode at 1550 nm.

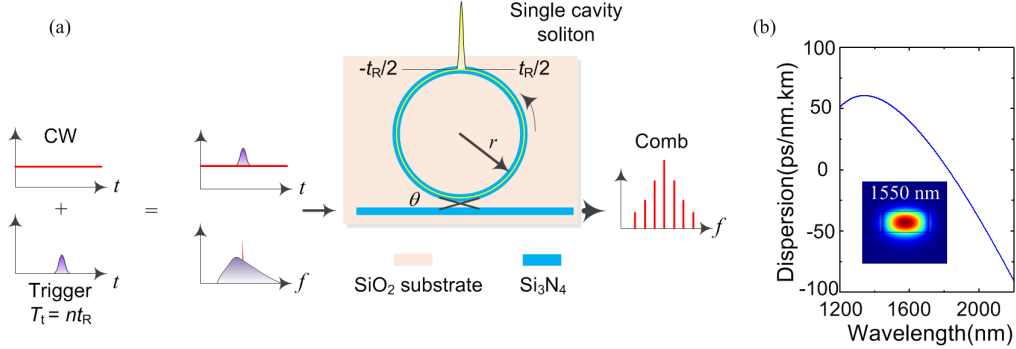


Figure 1 (a) Schematic diagram of the proposed single-soliton Kerr comb generation. (b) The dispersion profile as a function of wavelength. Inset, the electric field profile at 1550 nm.

The combined field of a CW pump and a low repetition rate pulse train is injected into the resonator. The pulses have a hyperbolic secant profile and a period of  $T_1 = nt_R$ , where  $n$  is an integer. The carrier frequency of the CW pump is fixed and red-shifted with respect to the closest cold-cavity resonant frequency. When the intracavity power accumulates by consecutive injection of the driving light, comb spectra can be generated by cascaded FWM. When the balance between gain and loss, and that between dispersion and nonlinearity are both established, localized dissipative structures, namely cavity solitons, will appear in the cavity. In our scheme, the short trigger pulse coupled into the cavity will inject energies into the comb lines that defined by the resonant frequencies of the cavity and covered by the trigger pulse spectrum. Most important, the phase of those seeded comb lines are intrinsically synchronized since they are generated from a single pulse. Such coherently seeded comb lines will accelerate and firmly determine the comb generation process by avoiding the random building up of pulses from MI. From the view point of mathematics, the joint force of the CW beam and the trigger pulls the system into the basin of attraction of the cavity soliton, which is one of the attractors of the nonlinear dynamical system. Thus it evolves into the single-soliton state directly without experiencing any complex dynamics.

In the proposed triggering scheme, the combined injection signal will vary significantly from roundtrip to roundtrip when the trigger pulse is launched, thus the mean-field Lugiato-Lefever equation (LLE) is no longer adequate to describe the system. We model the evolution of the optical field inside the microring with the Ikeda map [38,39],

$$\psi^{(m+1)}(z=0, \tau) = \sqrt{\theta} \psi_{\text{in}}^{(m)}(\tau) + \sqrt{1-\theta} e^{-i\delta_0} \psi^{(m)}(z=L, \tau), \quad (1)$$

$$\frac{\partial \psi^{(m)}(z, \tau)}{\partial z} = -\frac{\alpha_0}{2} \psi^{(m)} + i \sum_{k \geq 2} \frac{\beta_k}{k!} \left( i \frac{\partial}{\partial \tau} \right)^k \psi^{(m)} + i\gamma (1 + i\tau_{\text{shock}} \frac{\partial}{\partial \tau}) |\psi^{(m)}|^2 \psi^{(m)}, \quad (2)$$

where  $\psi^{(m)}(z, \tau)$  is the slowly-varying envelope of the intracavity optical field in the  $m$ -th roundtrip,  $\tau$  is the time retarded by the group velocity delay,  $\alpha_0$  is the linear loss coefficient,  $\theta$  is the coupling coefficient between the microring and the bus waveguide,  $\beta_k$  is the  $k$ -th order dispersion coefficient,  $\gamma$  is the nonlinear coefficient,  $L = 2\pi r$  is the roundtrip length,  $r$  is the radius of the microring,  $\delta_0 = t_R(\omega_p - \omega_b) = 2\pi l - \phi_0$  is the detuning between the CW pump frequency  $\omega_p$  and its closest  $l$ -th order cold-cavity resonant frequency  $\omega_b$ ,  $\phi_0$  is the linear phase delay of the intracavity field in a single roundtrip, and  $\tau_{\text{shock}} = 1/\omega_b$  is the optical shock time constant. The dispersion of nonlinearity was found to be negligible in  $\text{Si}_3\text{N}_4$  microring resonator [17,18,40]. The combined pump  $\psi_{\text{in}}^{(m)}$  at  $m$ -th roundtrip is given by,

$$\psi_{\text{in}}^{(m)}(\tau) = \psi_{\text{cw}} + \sqrt{P_t} \exp[-i\Delta\Omega(\tau + mt_R)] \sum_{p=0}^{N-1} \text{sech}[(\tau + mt_R - pT_t)/\tau_t], \quad (3)$$

where  $\psi_{\text{cw}}$  is the CW pump field,  $P_t$  and  $\tau_t$  are the peak power and width of the trigger pulse, respectively.  $\Delta\Omega = 2\pi\Delta f = 2\pi(f_t - f_{\text{cw}})$  is the central frequency offset of the trigger with respect to the CW pump.  $f_t$  and  $f_{\text{cw}}$  are the central frequencies of the trigger and the CW fields, respectively.  $T_t = 1/R_t$  is the period of the trigger and  $R_t$  is the repetition rate of it.  $N$  is the number of consecutive trigger pulses injected into the cavity. Equation (3) fully defines the fast variation of the combined injection signal from roundtrip to roundtrip.

Importantly, the intrapulse Raman scattering and thermal effects will more or less affect the building up of SCS, but will not destroy the transient generation process. Therefore, we first study the characteristics of the trigger approach on SCS generation without including the intrapulse Raman scattering and thermal dynamic in Equations (1) and (2). Alternatively, the intrapulse Raman scattering and thermal effects will be considered as perturbations to the system and discussed in Section 4.

### 3. PERFORMANCES OF THE SINGLE-SOLITON KERR COMB

#### 3.1 Low speed pulse train trigger

The low speed pulse train defined here refers to a pulse train whose repetition rate is an integer fraction of the FSR of the microresonator. We solve Equations (1) and (2) iteratively using the split-step Fourier method. The power of the CW pump is 1 W. The pump frequency is fixed at 193.413 THz, which is 730 MHz offset from the closest cold-cavity resonance. Thus, the detuning is fixed at  $\delta_0 = 0.0204$ . Higher-order dispersion parameters, up to the 12-th order, are considered. We first choose a repetition rate of the trigger as  $R_t = \text{FSR}/2^7 \approx 1.77$  GHz. In simulations, hyperbolic secant pulse triggers are switched on in the first  $2^{13}$  roundtrips and then switched off in the following roundtrips. Figure 2(a) shows the temporal evolution of the intracavity fields. The inset on the left side of Figure 2(a) depicts which roundtrips the triggers were turned on. Figures 2(b) and 2(c) show the instantaneous temporal profiles at the final and the  $2^{13}$ -th roundtrips, respectively. We observe that an SCS superimposed on a CW background is excited at  $\sim 2300$ -th roundtrip after a short period of FWM spectrum expansion starting from the initial comb lines introduced by the trigger pulse. The soliton experiences transient oscillation and eventually evolves to a “stable” state. Figure 2(d) shows the corresponding spectral evolution during the formation of the SCS. We note the state is almost stationary but with some minor fluctuations before the switching off of the trigger pulse. Such minor fluctuations can be seen from the CW background in Figure 2(c) and the borders of spectrum in Figure 2(f). When the trigger is switched off, the soliton evolves into a stable state and generates a smooth sech-shaped spectral envelope, as shown in Figures 2(b) and 2(e). The final cavity soliton has a peak power of 86.2 W and full width at half maximum (FWHM) of 43.2 fs. Figures 2(g) and 2(h) show the detailed temporal and spectral

profiles of the combined pump field spanning 4 roundtrip times. We note that the interference-induced oscillation of the envelope spreads out of a single roundtrip time slot, which has been considered in our simulations through the definition of Equation (3).

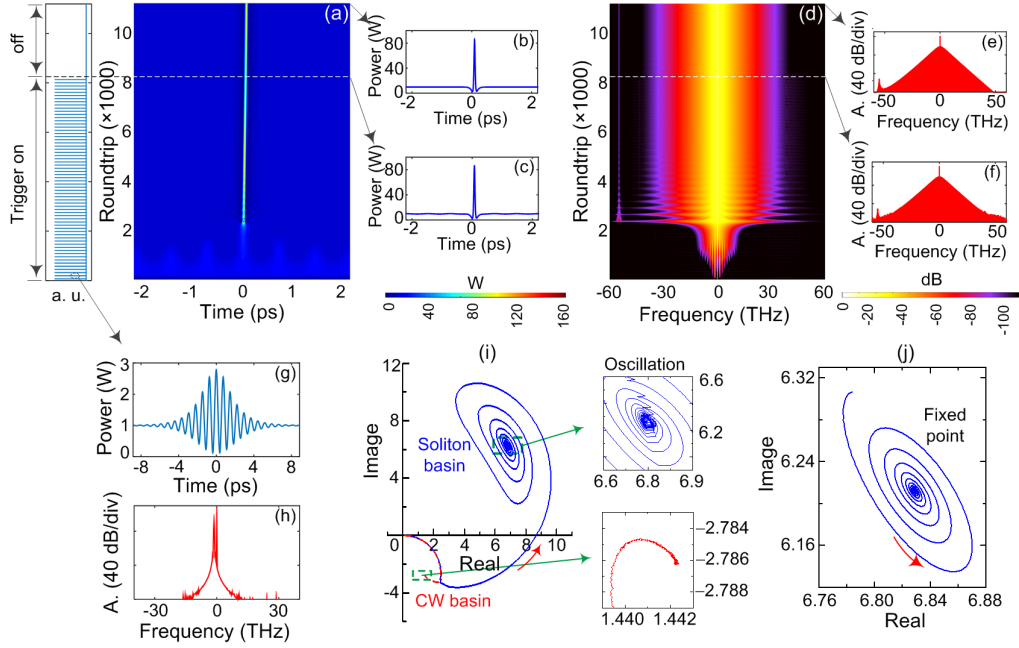


Figure 2 (a) Temporal evolution of the intracavity fields. The instantaneous temporal profiles at the (b) final and (c)  $2^{13}$ -th roundtrip, respectively. (d) Spectral evolution of the intracavity fields. The instantaneous spectral profiles at the (e) final and (f)  $2^{13}$ -th roundtrip, respectively. The (g) temporal and (h) spectral profiles of the combined pump field spanning 4 roundtrip time, respectively. The trajectories (blue solid lines) of the maximum peak power point of the intracavity fields in the complex plane with trigger, (i) when the trigger is switched on, and (j) after the trigger is switched off. The trajectories (red dashed lines) without any trigger are also shown in (i). Upper inset of (i): the zoom-in views close to the soliton fixed point regions. Lower inset of (i): CW fixed point regions. Other parameters:  $P_t = 0.45$  W,  $\tau_t = 1.5$  ps,  $\Delta f = -6 \cdot \text{FSR} = -1.356$  THz,  $\gamma = 1$  W<sup>-1</sup>/m,  $L = 628$   $\mu$ m,  $\alpha_0 L = 0.012$ , and a loaded  $Q \approx 1 \times 10^5$ .

We also track the temporal evolution of the maximum peak power point of the intracavity fields and show the trajectories in the complex plane. The blue solid curves in Figures 2(i) and 2(j) show the trajectories with the pulse trigger when the trigger is switched on, and after the trigger is switched off, respectively. The red dashed lines in Figure 2(i) show the trajectories without the pulse trigger. From Figure 2(i), we observe that initially when the intracavity energy is low, even in the presence of the trigger the intracavity fields evolve towards the CW state which is a fixed point of the dynamical system. As the intracavity energy accumulates, the optical fields assisted by the pulse triggers generate sufficiently large Kerr phase shift exceeding the detuning-induced phase shift to abruptly pull the dynamical system towards the SCS fixed point, which manifests as a kink in the trajectories. In other words, the intracavity fields are pulled from the basin of attraction of the CW fixed point to that of the soliton fixed point. In comparison, we show the trajectories (red dashed curves) of the intracavity fields without any trigger assistance. We observe there is no kink in the trajectories and the intracavity fields are pulled into the CW fixed point directly. The upper inset of Figure 2(i) clearly shows the existence of pulse triggers induces perturbations to the convergence around the fixed point. Figure 2(j) shows the fixed point can be reached after the trigger is switched off.

### 3.2 Impacts of trigger parameters

In applications, the parameters of the pulse train are determined by the laser sources, which can vary significantly in different laboratories. The impacts of the trigger parameters, e.g.  $P_t$ ,  $\tau_t$ ,  $R_t$  and  $\Delta f$ , on the performances of the intracavity temporal profiles will be investigated in this section.

First, we investigate the minimum required peak power  $P_{t\_min}$  of the trigger for SCS generation versus the repetition-rate  $R_t$  of the triggers. Figure 3 plots  $P_{t\_min}$  versus  $R_t$  in logarithmic scale under different trigger pulse width  $\tau_t$ . We note that all three curves are approximately straight lines with the slopes  $-1.92$ ,  $-1.93$ , and  $-1.93$  for  $\tau_t = 1.5$ ,  $1.0$ , and  $0.5$  ps, respectively, which suggests the inverse square law dependence of  $P_{t\_min}$  on  $R_t$ . In other words,  $P_{t\_min}$  will be reduced by four times and the average power will be reduced by half if  $R_t$  is doubled. For example, as  $\tau_t$  is  $0.5$  ps, when  $R_t$  is increased from  $7.06$  to  $14.12$  GHz,  $P_{t\_min}$  is decreased from  $0.046$  to  $0.0114$  W. The relation however deviates somewhat when  $\tau_t$  and  $R_t$  are both large. Such deviation is because of the interference between the tails of adjacent trigger pulses since the period of the pulse train is already comparable to the pulse duration.

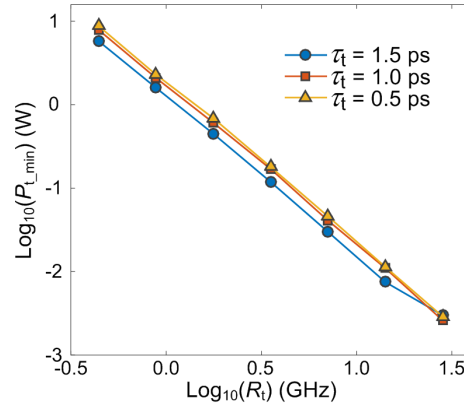


Figure 3 Minimum required peak power  $P_{t\_min}$  for SCS excitation versus the trigger repetition-rate  $R_t$  at different trigger width  $\tau_t$ .

To excite SCS in the cavity, the peak power should be larger than  $P_{t\_min}$ , but it should not be too large, otherwise multiple solitons will be excited. The effects of the trigger parameters, e.g.  $P_t$ ,  $\tau_t$ , and  $\Delta f$ , on the performances of the intracavity temporal profiles are investigated by changing one of the parameters while keeping the others constant. Figure 4(a) shows that multi-solitons could be generated when  $P_t$  exceeds  $0.5$  W, with  $\tau_t = 1.5$  ps,  $\Delta f = 6 \cdot \text{FSR}$  and  $R_t = 1.77$  GHz. The uniformly separated solitons have identical peak power and width with respect to the single-soliton state. Figure 4(b) shows that multi-solitons are also observed when the trigger pulse duration  $\tau_t$  is increased. Such multi-solitons excitation is possible when the power of the multiple peaks on the oscillating pump signal, as shown in Figure 2(g), exceeds the threshold of SCS excitation. Increasing either the trigger pulse duration or the peak power will have similar effect. We observe that six solitons with an uniform temporal interval of  $t_R/6$  are generated when  $\tau_t$  is larger than  $1.8$  ps, which means the Kerr comb generated has uniform frequency spacing of  $6 \cdot \text{FSR}$  that accordant to  $\Delta f$ . This property can be used to increase the repetition rate of the SCS using the same microring resonator. Moreover, the average power of the  $n$ -soliton state is  $n$  times that of the single-soliton state, which can generate much stronger comb intensity. We also note that cavity soliton is not excited when  $\tau_t$  is reduced to  $1.4$  ps, at which the trigger cannot provide enough energy to form the cavity solitons. Thus the excitation of the cavity soliton depends not only on the peak power but also the pulse energy. Such limitation can be understood with the evolution of

spectrum. If the trigger pulse becomes shorter, the spectrum will cover more comb lines but with smaller total energy, which will significantly reduce the intensity of each comb line and further degrade the FWM. Thus properly chosen trigger pulse duration and peak power are important to guarantee a SCS excitation.

Figure 4(c) shows the intracavity temporal profiles obtained with different  $\Delta f$ . We note that the results are symmetric with respect to  $\Delta f$ . Single-soliton state exists within certain range of  $\Delta f$ , i.e.  $\Delta f = \pm 3 \cdot \text{FSR}$ ,  $\pm 5 \cdot \text{FSR}$ , and  $\pm 6 \cdot \text{FSR}$  in this case. When  $\Delta f$  is out of this range, either CW state or multi-solitons states are excited. However, the multi-solitons state with  $\Delta f = \pm 4 \cdot \text{FSR}$  is different to those with  $\Delta f = 0, \pm 1 \cdot \text{FSR}$  and  $\pm 2 \cdot \text{FSR}$ . In the region of  $|\Delta f| < 3 \cdot \text{FSR}$ , the oscillating period of the combined pump signal is large. With sufficient energy and a broad pulse profile, modulation instability will dominant to generate pulses, which are observed as the closely but not identically separated pulses. With the increase of  $|\Delta f|$ , the period of the oscillation will decrease, which will decrease the modulation instability and only one pulse is observed with  $|\Delta f| = 3 \cdot \text{FSR}$ . With the increase of  $|\Delta f|$ , the peak power of the side lobes will also increase since they will be closer to the center of the pulse. Thus at  $|\Delta f| = 4 \cdot \text{FSR}$ , three cavity solitons are observed since the three peaks on the oscillating pump have become strong enough. But on another side, the energy confined in each side lobes will decrease along the increase of  $|\Delta f|$  since the duration of each lobe will decrease. Because of the joint contribution of the peak power and the single lobe energy, only one soliton is observed in the results with  $|\Delta f| = 5 \cdot \text{FSR}$  and  $6 \cdot \text{FSR}$ . When  $|\Delta f|$  is increased to  $7 \cdot \text{FSR}$ , even the main lobe of the oscillating pump cannot offer enough energy to trigger the soliton, thus no soliton is excited.

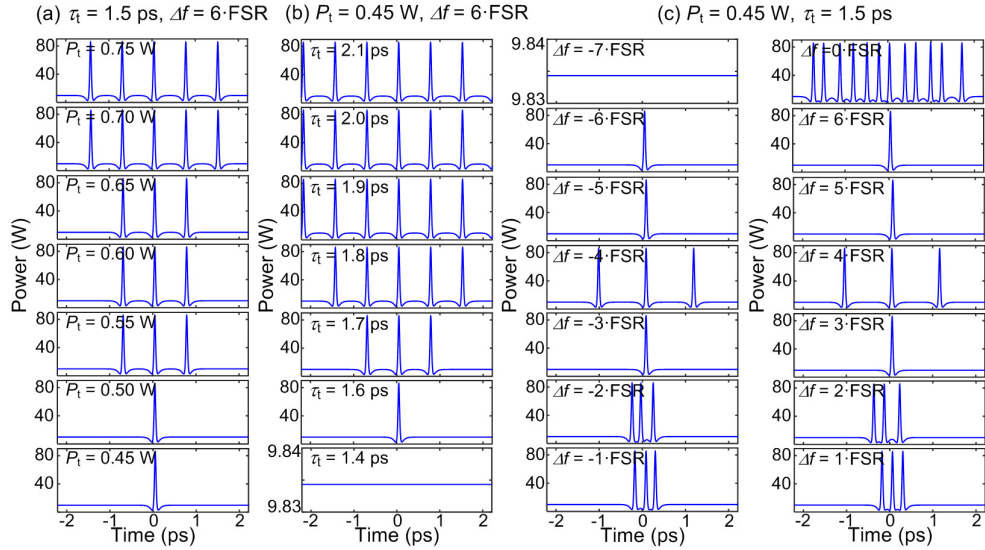


Figure 4 Impacts of the trigger parameters (a)  $P_t$ , (b)  $\tau_t$ , and (c)  $\Delta f$  on the performances of the intracavity temporal profiles.

In experiments, it is normally hard to perfectly synchronize the trigger pulse train to the cavity roundtrip time. The misalignment will affect the generation of the single-soliton Kerr comb. In frequency domain, the situation is equivalent to the mismatch between the spacing of the frequency comb lines of the trigger and the resonance frequencies of the microresonator. The out-of-synchronization parameter is defined by  $\Delta t = T_t - M \cdot t_R$ , where  $M = \lfloor T_t/t_R + 1/2 \rfloor$  estimates the closest integer ratio of the two periods. The central positions of the successively injected trigger pulses therefore get temporal delays of  $\Delta t, 2\Delta t, 3\Delta t, \dots$ , respectively. For each given  $M$ , there is a limited

interval of  $\Delta t \in [\Delta t_{\min}, \Delta t_{\max}]$ , where  $\Delta t_{\min} < 0$  and  $\Delta t_{\max} > 0$ , in which the single-soliton state can be maintained. We define the out-of-synchronization tolerance as  $\kappa = \Delta t_{\max} - \Delta t_{\min}$ , and the relative tolerance as  $\varepsilon = \kappa / M \cdot t_R$ . Figure 5(a) shows  $\kappa$  and  $\varepsilon$  as a function of  $\log_2(M)$  at three different trigger widths. The trigger peak power used for each case is the minimum power threshold for SCS generation. We observe that the magnitudes of  $\kappa$  increase monotonically when  $M$  is increased at all of the three cases studied. For example, when  $\tau_t$  is 1.5 ps,  $\kappa = 32.5$  and 68 fs are obtained at  $M = 7$  and 8, respectively. This is because when  $M$  increases, i.e. the speed of the trigger pulse train coming into the cavity becomes slower, the accumulation of the temporal delay decreases relatively within the same trigger injection time. We also observe that the triggers with larger pulse widths show larger out-of-synchronization tolerances. The percentage tolerance  $\varepsilon$  obtained at the three trigger widths are all at order  $10^{-5}$ . We observe that the relative tolerance does not vary monotonically with  $M$ , but increases monotonically with the increase of trigger width at a given  $M$ .

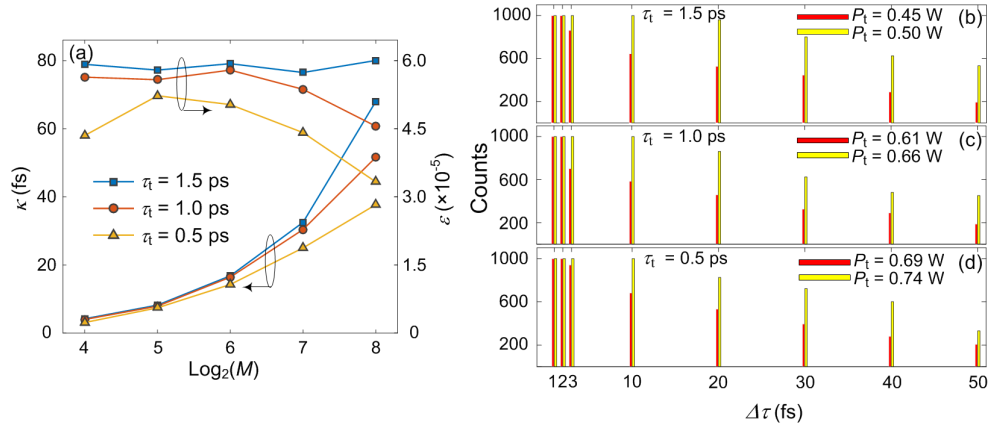


Figure 5 (a) Out-of-synchronization tolerance  $\kappa$  and relative tolerance  $\varepsilon$  as a function of  $\log_2(M)$  at different trigger pulse widths. (b) Counts of SCS generated of 1,000 statistical results as a function of the timing jitter  $\Delta\tau$  at different  $\tau_t$  and  $P_t$ .

Timing jitter of the trigger pulses is also a practical issue that might affect SCS generation. We assume that the random timing jitter of the trigger pulses satisfies a normal distribution with a zero mean value and a standard deviation  $\Delta\tau$ . We inject 500 consecutive trigger pulses at a repetition rate of 1.77 GHz into the cavity, which has an operation time of  $\sim 0.3$   $\mu$ s ( $\sim 64,000$  roundtrips). Figures 5(b)-5(d) show the statistical counts of successful SCS formation in each 1,000 simulations with a given  $\Delta\tau$ . The timing jitter is varied from 1 fs to 50 fs. Three different pulse trigger width  $\tau_t$  of 1.5, 1.0, and 0.5 ps are investigated respectively. At first, the trigger peak power is assumed to be the minimum threshold for SCS generation, i.e.  $P_t = 0.45$ , 0.61, and 0.69 W, respectively. We observe that the counts of successful SCS formation are 1,000 for all the three cases studied when  $\Delta\tau < 3$  fs, but decrease monotonically when  $\Delta\tau \geq 3$  fs. For example, when  $\Delta\tau$  equals to 3 fs, the counts at  $\tau_t = 1.5$ , 1.0, and 0.5 ps are 862, 702, and 942, respectively. When  $\Delta\tau$  is increased from 10 to 50 fs, the counts decrease from 554 to 153 at  $\tau_t = 1.5$  ps. We note that  $\tau_t$  and the counts do not have a monotonic relationship, e.g. the counts obtained at  $\tau_t = 1.0$  ps is smaller than that at  $\tau_t = 0.5$  ps and  $\tau_t = 1.5$  ps. Thus, the tolerance of timing jitter cannot be enhanced by simply increasing the trigger width. The reason is that the dependence of the beating product of the CW and pulse trigger, on the pulse trigger width, is rather complex, certainly not monotonic. In comparison, the trigger peak power of the three cases is slightly increased to  $P_t = 0.5$ , 0.66, and 0.74 W, respectively. The increased trigger power still satisfies SCS generation and will not lead to multi-solitons generation. Figures 5(b)-5(d) show the statistical results

in yellow bars. We observe that the error free timing jitter tolerances are all improved to more than ten femtoseconds. The results indicate that the tolerance of timing jitter can be enhanced by increasing the trigger peak power over the minimum thresholds for SCS generation.

Besides the trigger pulse train, the CW pump is also important. The SCS generation at different CW power is investigated accompanying by a trigger pulse train with a repetition rate of 1.77 GHz. The trigger pulse width and frequency offset are the same as that in Figure 2. We find that there exists a minimum detuning  $\delta_0$  to ensure SCS generation at a given CW pump power  $P_{cw}$ . If the detuning is below this value, the intracavity field will evolve into unstable MI or chaotic states, despite of the presence of triggers. For each combination of  $(\delta_0, P_{cw})$ , there exists a corresponding minimum trigger peak power  $P_t$  for SCS generation. Figure 6(a) shows the pairs of  $\delta_0$  and  $P_t$  when  $P_{cw}$  is increased from 0.65 to 1 W. We note that it is difficult to excite the SCS state when  $P_{cw} < 0.65$  W or  $> 1$  W because 0.65 and 1 W are close to the upper and lower inflection points of the bistable curves of stationary CW solutions of Equations (1) and (2) for the microresonator used. It is known that the cavity solitons exist almost, but not exactly, within the same bistable region of the stationary CW solutions [35,37,41], thus we can approximately estimate the valid region of  $P_{cw}$ . When  $\delta_0$  increases from  $\delta_0$ ,  $P_t$  that required to excite SCS state will also increase. Figure 6(b) shows the different operation regions with different  $P_t$  and  $\delta_0$  when  $P_{cw}$  is 1 W. When  $\delta_0$  is increased from 0.0204 to 0.03, there is always a band bounded by the blue dashed curves that ensures the generation of stable SCS. Parameter combinations within the region above the band will lead to stable multi-solitons states. Only homogeneous CW states can be found in the region below this band. The inset shows the zoom-in view when  $\delta_0$  varies from 0.0204 to 0.021. We observe that larger  $\delta_0$  will give a broader range of  $P_t$  for SCS formation. However,  $\delta_0$  cannot increase indefinitely. Otherwise, there will not be a bistable region with the given  $P_{cw}$  and homogeneous CW or MI states will be found only.

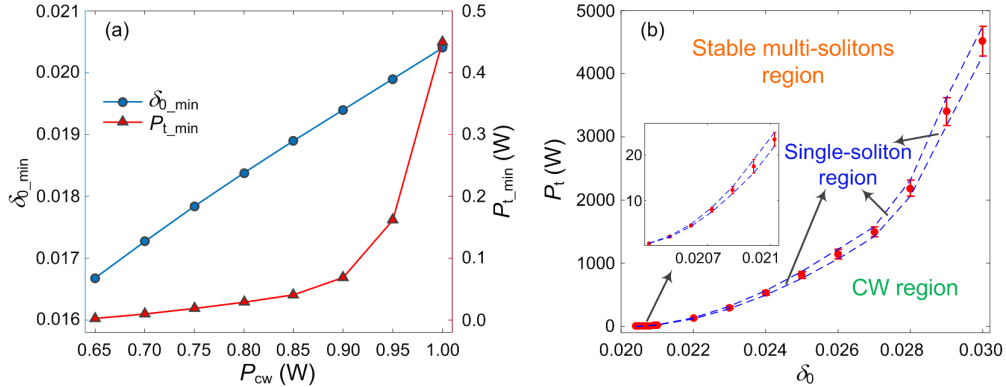


Figure 6 (a) Minimum required  $\delta_0$  and  $P_t$  for SCS generation at different  $P_{cw}$ . (b) Different operation regions within the parameter space of  $P_t$  and  $\delta_0$  at  $P_{cw} = 1$  W. Inset: zoom-in view of  $\delta_0 \in [0.0204, 0.021]$ .

### 3.3 Single shot pulse trigger

In addition to the synchronization and timing jitter problem discussed in 3.2, the CEP of the pulse train trigger source should also be stabilized to guarantee a fixed detuning. The pulse train trigger can work only when the above problems are overcome. Obviously, it is rather difficult to find such highly stable pulse train sources right now to serve as the trigger. Fortunately, we find that it is also possible to excite the SCS state by just using a single shot pulse trigger. The finding is important as single shot pulse trigger has the obvious advantages that none of the synchronization, timing jitter, and CEP stabilization problems will arise. Such single shot pulse trigger scheme can be considered as an extremely long period pulse train triggering where the period of pulse train is much longer than the

excitation time of the SCS (typically several nanoseconds). When a single shot pulse trigger is sufficient to excite the SCS, we can switch off the trigger laser source after a single pulse is injected into the cavity. Thus any low repetition rate pico- or femto-second lasers with sufficient peak power and single pulse energy can be used to kick start the microring resonator to reach the SCS state. In simulations, the parameters used are the same as that in Figure 2 except for the peak power and detuning. The detuning is fixed at  $\delta_0 = 0.0205$  here. A single shot pulse with a peak power of 520 W is launched at the 2050-th roundtrip, accompanying the always existent CW pump, as shown in the inset of Figure 7(a). After the injection of the trigger pulse, several weak pulses appear in the cavity and finally the central one evolves to a stable SCS. Figure 7(b) shows the instantaneous intracavity temporal profile at the final roundtrip. An SCS with a peak power of 86 W and an FWHM of 43.4 fs is obtained. Figure 7(c) shows the instantaneous intracavity temporal profile at the 3084-th roundtrip, which is at the first peak position of a damped oscillation along the propagation. The cavity soliton has a higher peak power of 143 W and a smaller FWHM of 32 fs comparing to the final state. Figures 7(d), 7(e), and 7(f) show the spectral evolution, instantaneous spectral profiles at the final and the 3084-th roundtrips, respectively. From Figure 7(d), an initial broadband gain is introduced by the high energy single shot pulse trigger, which forces and accelerates the generation of the cavity soliton. Both the evolutions of temporal profile and spectrum of the cavity field are similar to that shown in Figure 2 with periodic pulse train trigger, except for the slight difference just after the launch of the single shot pulse trigger.

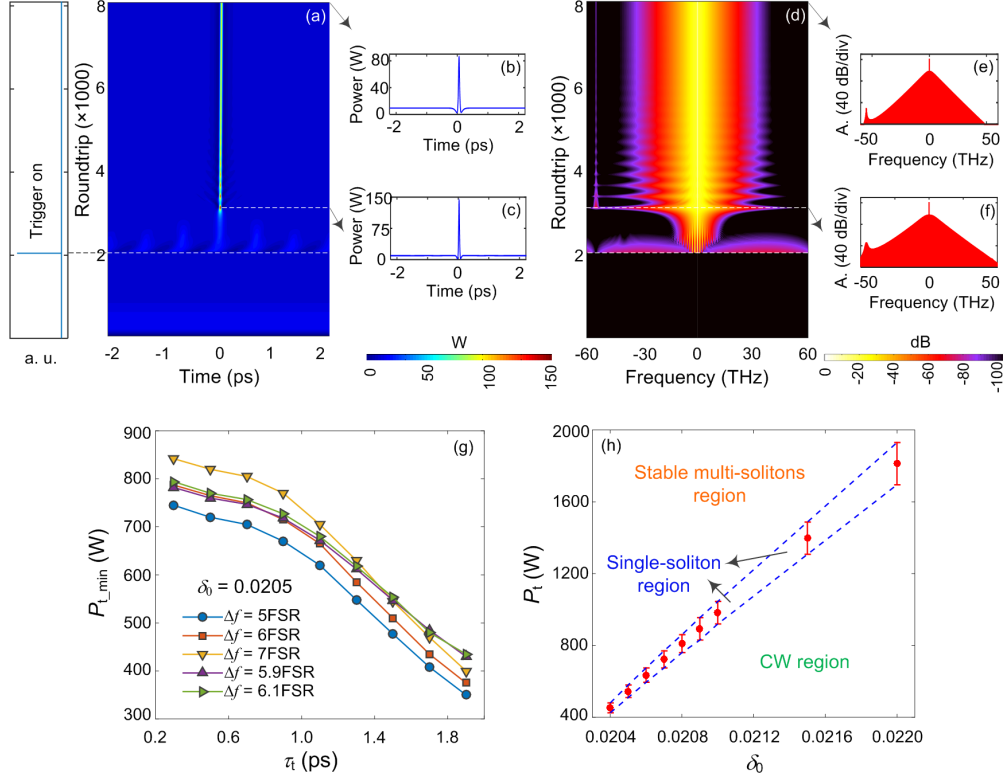


Figure 7 (a)-(c) Temporal and (d)-(f) spectral evolutions of the intracavity field and the instantaneous profiles at the final and 3084-th roundtrips, respectively, when a single shot trigger with a peak power of 520 W and an FWHM of 1.5 ps is injected. (g)  $P_{t,min}$  as a function of  $\tau_t$  at different  $\Delta f$ .  $\delta_0$  is fixed at 0.0205. (h) Different operation regions within the parameter space of  $P_t$  and  $\delta_0$  with  $\tau_t = 1.5$  ps and  $\Delta f = 6 \cdot \text{FSR}$ .

We note that multi-solitons states similar to that in Figure 4 can also be excited when the parameters of the single shot pulse trigger are varied. The dependence of the SCS generation on the trigger parameters  $P_t$ ,  $\tau_t$ , and  $\Delta f$  is similar to that with a pulse train trigger. Figure 7(g) shows the minimum  $P_t$  for SCS generation as a function of the trigger pulse width  $\tau_t$  at different central frequency offset  $\Delta f$  for single shot pulse trigger. The required  $P_{t\_min}$  decreases when  $\tau_t$  increases.  $P_{t\_min}$  is found to be 510 W when  $\tau_t = 1.5$  ps and  $\Delta f = 6 \cdot \text{FSR}$ , which are used for Figures 7(a)-(f). For those  $\Delta f$  values as integer multiples of the FSR, a larger  $\Delta f$  corresponds to a larger  $P_{t\_min}$ . Such relationship is reasonable since larger  $\Delta f$  will narrow the period of the beating oscillation of the trigger and the CW pump, thus reduce the energy of each peak. To compensate the energy reduction,  $P_{t\_min}$  should be increased for larger  $\Delta f$ . When  $\Delta f$  deviates a little from integer multiples of the FSR, e.g.  $\Delta f = 5.9 \cdot \text{FSR}$  and  $6.1 \cdot \text{FSR}$ ,  $P_{t\_min}$  deviates from the original curve especially when  $\tau_t$  is larger than 1 ps. The deviation of  $\Delta f$  will break the matching of the oscillation period and the roundtrip time, which will lead to destructive perturbation caused by the coherent stacking of pulse trials that leaked into the adjacent roundtrips. Such perturbation will increase severely when the trigger pulse becomes longer. Thus the pulse trigger should not be too long, otherwise extra power will be required to overcome the perturbation from the “pulse folding”. For example, with a trigger pulse width of 1.5 ps, the power threshold increases  $\sim 40$  W when  $\Delta f$  varies in a range of  $\pm 0.1 \cdot \text{FSR}$  from  $6 \cdot \text{FSR}$ . Within the same variation range of  $\Delta f$ , the power penalty is only  $\sim 5$  W with a 0.5 ps trigger pulse. With a 0.5 ps trigger, the SCS state can be excited even at  $\Delta f = 5.5 \cdot \text{FSR}$ , i.e. the frequency deviation is at the maximum of  $0.5 \cdot \text{FSR}$ , with the same  $P_{t\_min}$  as that at  $\Delta f = 6.0 \cdot \text{FSR}$ . Thus, with an ultrashort trigger pulse, the SCS excitation is insensitive to the frequency detuning of the single shot trigger pulse. From Figure 7(g), we find that the curves of  $\Delta f = 5.9 \cdot \text{FSR}$  and  $6.1 \cdot \text{FSR}$  begin to deviate from that of  $\Delta f = 6.0 \cdot \text{FSR}$  when  $\tau_t$  is about 1 ps. Thus, the best choice of the trigger pulse width should be  $< 1$  ps within the proposed microresonator. Figure 7(h) shows the working regions of  $P_t$  and  $\delta_0$  at  $\tau_t = 1.5$  ps and  $\Delta f = 6 \cdot \text{FSR}$ , which is obtained similar to Figure 6(b) but with a single shot pulse trigger. The minimum  $\delta_0$  is found to be also 0.0204, which is consistent with that in Figure 6(a). Similar to the results in Figure 6(b), the two blue dashed curves divide the parameter space into stable multi-solitons (upper), SCS (middle band), and CW state (lower) regions. However, unlike Figure 6(b), the boundaries of the three operation regions, i.e. the two blue dashes curves, are almost straight lines in Figure 7(h).

The single shot pulse trigger requires higher peak power for SCS generation when compared to a pulse train trigger but it does not increase the requirement to the average power of the trigger source since the repetition rate can be greatly reduced. Furthermore, out-of-synchronization, timing jitter, and CEP-stabilization are no longer required. A single shot pulse trigger also makes it feasible to manipulate the number and temporal locations of the cavity solitons generated by varying the peak power and temporal location of the trigger pulse. Such simple and robust SCS excitation scheme is potentially to be adopted for realizing ultrahigh-speed optical memory in monolithic microresonators.

## 4. DISCUSSION

### 4.1 Deterministic SCS generation

SCS generation using the conventional frequency tuning approach is not completely deterministic because the intracavity field must undergo the chaotic state before the SCS state can be reached [14,18,25]. We compare the conventional pump frequency tuning approach with the proposed single shot pulse trigger approach by introducing temporal perturbations to the driving field. The perturbation is defined as  $\sigma = \eta \hat{N} \exp(i2\pi \hat{U})$ . Here  $\hat{N}$  is a normally distributed random variable with zero mean value and standard deviation of 1,  $\hat{U}$  is a uniformly distributed random variable between 0 and 1, and

$\eta = 1 \times 10^{-8}$  is the factor denoting the amplitude of the perturbation. The other parameters used in both cases are the same as those in Figure 2 except for the detuning parameter  $\delta_0$  and the perturbation to the driving field.

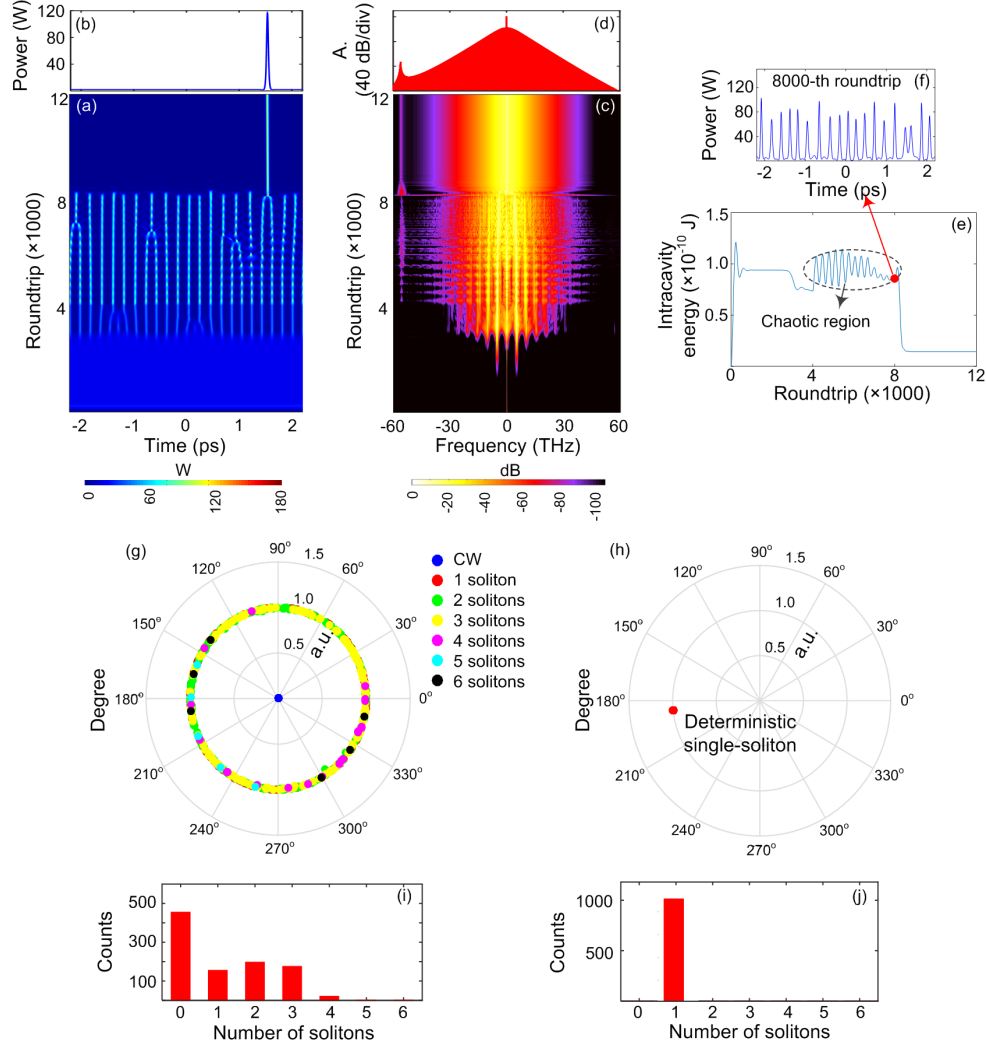


Figure 8 (a)-(b) Temporal and (c)-(d) spectral evolutions of the intracavity field and the instantaneous profiles at the final roundtrip. (e) The intracavity energy at each roundtrip. (f) Instantaneous temporal profile at the 8000-th roundtrip of the pump frequency tuning approach. 1,000 simulation results using (g) the pump frequency tuning and (h) the proposed trigger approaches, respectively. The counts of different soliton states of the 1,000 simulations using (i) the pump frequency tuning and (j) the trigger approaches, respectively.

Figures 8(a) and 8(c) show the temporal and spectral evolutions of the pump frequency tuning approach, respectively. Figures 8(b) and 8(d) show the instantaneous temporal and spectral profiles at the final roundtrip, respectively.  $\delta_0$  is initially set to 0.005, and increased to 0.018 and 0.035 at the 4000-th and 8000-th roundtrips, respectively. We observe that the intracavity field experiences unstable modulation instability and chaotic state before the SCS is excited. The multi-solitons states could also be excited if an intermediate  $\delta_0$  between 0.018 and 0.035 was used after the chaotic state. Figure 8(e) shows the evolution of the total intracavity energy along the dynamics. The chaotic region is clearly indicated by the large oscillations of the energy. Figure 8(f) shows the instantaneous temporal profile at the 8000-th roundtrip, which presents a group of pulses with random-like locations and amplitudes in

the chaotic state. We carry out 1,000 simulations for the pump frequency tuning and trigger approaches, and plot the temporal positions and peak power of the solitons in Figures 8(g) and 8(h), respectively. The temporal positions of the cavity solitons at the final roundtrip, which are in the range of  $[-t_R/2, t_R/2]$ , are mapped into the angular position  $[0^\circ, 360^\circ]$ . The peak power is normalized to the maximum peak power of the single-soliton case and indicated by the radial position. Figure 8(g) shows the results of the 1,000 simulations when the pump frequency tuning approach is used. The angular positions of all the multi-solitons generated are recorded. We observe that the final soliton states are not deterministic. The number of the solitons excited varies from zero to six. Even homogeneous CW states are observed. In contrast, as shown in Figure 8(h), the simulation results of the proposed trigger approach are deterministically single-soliton state. Figures 8(i) and 8(j) show the counts of different soliton states of the pump-tuning and trigger approaches, respectively. It is surprising that homogeneous CW state without any soliton is the mostly observed one in the pump frequency tuning approach. The count of single-soliton in the pump frequency tuning approach is only 154 out of 1,000, while 1,000 is obtained in the proposed trigger approach.

#### 4.2 Influence of intrapulse Raman scattering

When the single shot high power ultrashort pulse is used to trigger the SCS, it is curious to know how will the intrapulse Raman scattering affect the dynamics since it can contribute much in ultrashort pulse dynamics such as supercontinuum generation. Broadband intrapulse Raman scattering (IRS) has been found to present in amorphous  $\text{Si}_3\text{N}_4$  material, which was considered in recent works of Kerr comb generation [42,43]. However, the significance of IRS in crystalline  $\text{Si}_3\text{N}_4$  is still unclear. Also, the IRS is confirmed to be negligible for TM-polarization mode in silicon-based materials [44,45]. Therefore, we treat IRS as perturbation and model it by adding the Raman terms in Equation (2),

$$\frac{\partial \psi^{(m)}(z, \tau)}{\partial z} = -\frac{\alpha_0}{2} \psi^{(m)} + i \sum_{k \geq 2} \frac{\beta_k}{k!} \left( i \frac{\partial}{\partial \tau} \right)^k \psi^{(m)} + i \gamma (1 + i \tau_{\text{shock}} \frac{\partial}{\partial \tau}) \left( \psi^{(m)} \int_{-\infty}^{\tau} R(\tau - \tau') |\psi^{(m)}(z, \tau')|^2 d\tau' \right), \quad (4)$$

where  $R(t) = (1 - f_R) \delta(t) + f_R h_R(t)$  is the nonlinear response function,  $h_R(t)$  is the Raman response function and  $f_R = 0.2$  is the fractional contribution of the nuclei to the total nonlinear polarization [42].

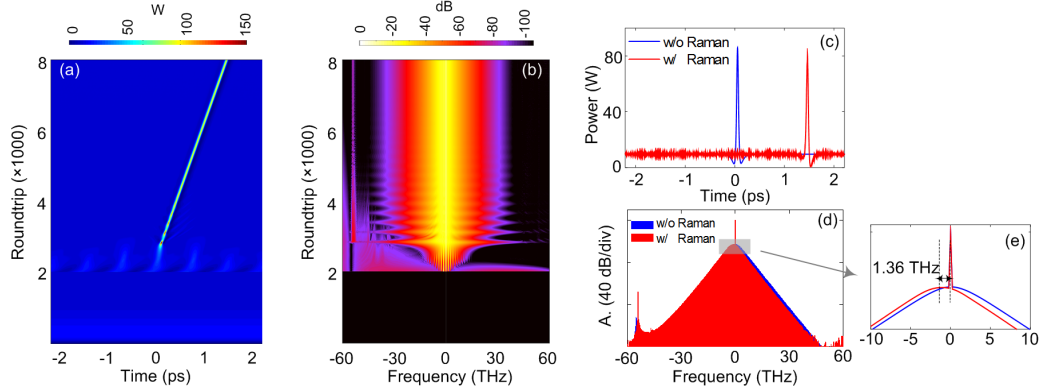


Figure 9 (a) Temporal and (b) spectral evolutions of the intracavity fields with IRS. Instantaneous (c) temporal and (d) spectral profiles at the final roundtrip with and without IRS. (e) Zoom-in view of the spectral envelopes at the central part of the spectra.

Figures 9(a) and 9(b) show the temporal and spectral evolutions of the intracavity fields, respectively. A single shot pulse trigger is used to excite the SCS. We observe that IRS does not affect the generation of the SCS, but induces obvious temporal delay to the SCS, which agrees with the intrinsic characteristics of IRS, under which the spectra of the soliton get red-shifted and the soliton

itself becomes slower than the reference group velocity of the pump field. Figure 9(c) shows the instantaneous temporal profiles at the final roundtrip with and without IRS. The SCS obtained with IRS has a peak power of 81.54 W and an FWHM of 45.1 fs, which are 4.46 W lower and 1.7 fs larger, respectively, than that without IRS. We note that the IRS induces rapid oscillations on the CW background. The dip in the leading edge of the SCS is also enhanced. We believe this is because the IRS red-shifts the spectra of the SCS towards the zero-dispersion wavelength, and thus enhances the effect of third-order dispersion. The third-order dispersion coefficient  $\beta_3$  in our work is negative so that the  $\beta_3$ -induced oscillation occurs on the leading edge of the soliton. Figure 9(d) shows the corresponding instantaneous spectral profiles with and without IRS. We observe that the SCS spectra with IRS are clearly red-shifted. The Cherenkov radiation is also enhanced by the IRS. Figure 9(e) shows the zoom-in view of the spectral envelopes at the central part of the spectra, in which we observe a 1.36 THz frequency red-shift of the SCS spectra.

### 4.3 Influence of trigger profiles

In the above simulations, hyperbolic secant pulse triggers with different parameters are investigated in the excitation of SCS. In applications, the waveform profiles generated by different laser sources can vary significantly. In this section, we will investigate the impact of trigger pulse profile on the SCS excitation. Gaussian and super Gaussian (2-nd order) pulses are considered to compare with hyperbolic secant pulse. Single shot pulse trigger approach is adopted here and the parameters used are the same as that in Figure 7 except the peak power of the trigger. Figures 10(a)-10(d) show the intracavity temporal evolution and instantaneous temporal profiles at the final roundtrip with Gaussian and super Gaussian pulse triggers. The dynamics are almost same to that observed with hyperbolic secant pulse. After the trigger is injected, the SCS state is directly excited without going through the chaotic states. The minimum peak powers  $P_{t\_min}$  to trigger the SCS are 720 and 755 W for Gaussian and super Gaussian pulses, respectively, both are larger than the 510 W of hyperbolic secant trigger. In addition, the super Gaussian pulse trigger takes a little longer time to excite the SCS than that with the Gaussian pulse trigger because it needs longer propagation to eliminate the stronger side lobes. Figure 10(e) shows the intracavity temporal interference profiles in three roundtrip time slots when the hyperbolic secant, Gaussian, and super Gaussian pulse triggers with a same peak power of 520 W and an FWHM of 1.5 ps are used. We observe that the hyperbolic secant pulse induces much stronger trails extending into the adjacent roundtrip time slots. These trails will contribute extra energy for SCS generation when interfered with the optical field in the central roundtrip time slot, thus reduce the peak power threshold. In comparison, the super Gaussian pulse induces very weak tails. Instead, two strong side lobes arise beside the central peak. The peak powers of these two side lobes are comparable to that of the central peak, thus they compete with the central peak during evolution and hamper the SCS formation. Figure 10(f) shows the corresponding spectral profiles of the three interfered fields. The shapes of the spectral envelopes are very different, e.g. the envelope of the super Gaussian pulse is modulated because of the two strong side lobes generated in the time domain. However, we note the SCS state can still be excited by all the pulse profiles studied if sufficient peak power of the pulse trigger is given. Thus the trigger profiles studied do not have significant impact on the proposed trigger approach.

Although the super Gaussian trigger requires the highest peak power for SCS generation, it has other advantages when compared to the hyperbolic secant and Gaussian profiles. The inset of Figure 10(f) shows that the  $-10$  dB bandwidths of the hyperbolic secant, Gaussian, and super Gaussian triggers are 241, 318, and 435 GHz, respectively. The broader bandwidth of the super Gaussian trigger makes it more tolerable to the frequency deviation discussed in Figure 7(g) if the pulse width is large.

Figure 10(g) shows the minimum peak power threshold  $P_{t,\min}$  for SCS generation as a function of  $\Delta f$  at different trigger profiles. The initial conditions of the three triggers are the same as that used in Figure 10(e). We define the frequency deviation here as  $|\Delta f - 6 \cdot \text{FSR}|$ . We observe that when the frequency deviation increases, the power thresholds of the hyperbolic secant trigger increase significantly when compared to that at  $\Delta f = 6 \cdot \text{FSR}$ . In comparison, the Gaussian trigger requires a smaller increase in the power thresholds for the same frequency deviation. The super Gaussian trigger requires the smallest increase in the peak power threshold when  $\Delta f > 6 \cdot \text{FSR}$ , and even a decrease in the threshold when  $\Delta f < 6 \cdot \text{FSR}$ . For example, when  $\Delta f$  is  $6.3 \cdot \text{FSR}$  (frequency deviation is  $0.3 \cdot \text{FSR}$ ), the increase of the power thresholds for hyperbolic secant, Gaussian, and super Gaussian triggers are 370, 65, and 15 W, respectively. The hyperbolic secant trigger requires the highest increase in the power threshold because its bandwidth is comparable with the FSR which is 226 GHz. In contrast, the bandwidth of the super Gaussian trigger is about twice the FSR, thus it has the highest tolerance to frequency deviation.

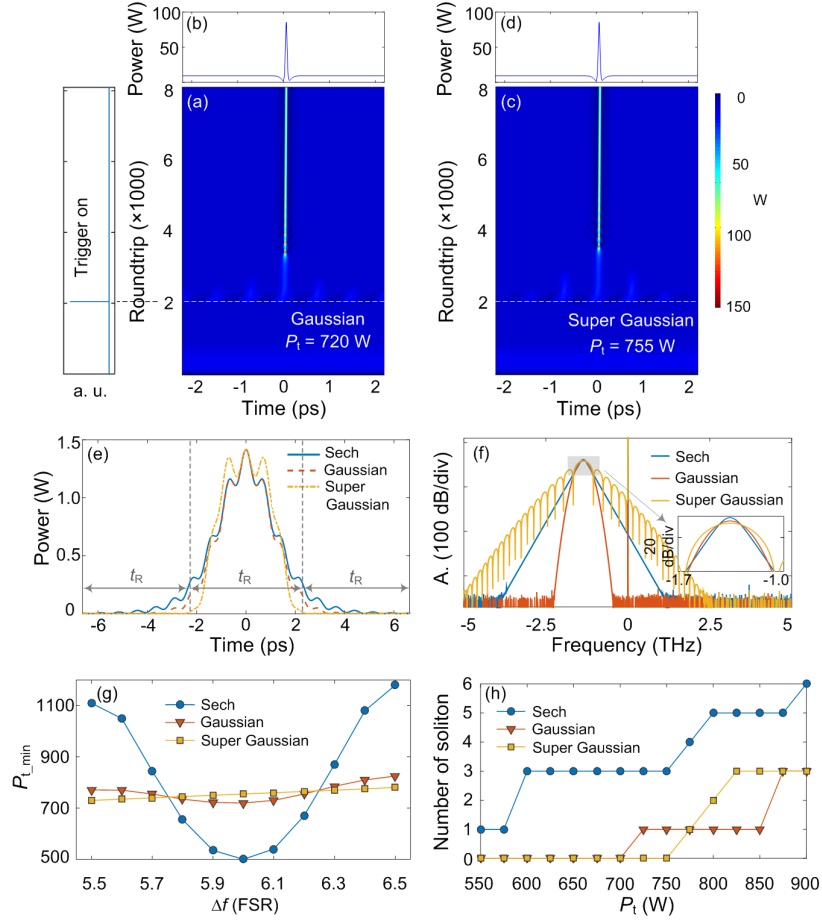


Figure 10 Intracavity temporal evolution and the instantaneous temporal profiles at the final roundtrip when Gaussian pulse trigger ((a) and (b)), and super Gaussian (2-nd order) pulse trigger ((c) and (d)) are used, respectively. The (e) temporal and (f) spectral profiles of the intracavity interfered fields between the pulse trigger and the CW pump fields. The hyperbolic secant, Gaussian, and super Gaussian triggers are studied using the same peak power of 520 W and FWHM of 1.5 ps. Inset in (f): The zoom-in view of the  $-30$  dB spectral profiles (g)  $P_{t,\min}$  as a function of  $\Delta f$  for different trigger profiles. (h) The number of solitons generated as a function of the trigger peak power  $P_t$  for different trigger profiles.

Figure 10(h) shows the number of solitons generated as a function of the trigger peak power  $P_t$  for

the three different trigger profiles. The FWHM of the trigger is 1.5 ps in all three cases. The transition curves of multi-solitons states are obtained using  $P_t$  values with a granularity of 25 W in the simulation. Thus the details of the transition between successive multi-solitons states are not shown. The frequency offset  $\Delta f$  is fixed at 6-FSR. From Figure 10(h), the pulse profiles affect the transitions to the single- and multi-solitons states. The hyperbolic secant trigger requires the lowest peak power to generate the single- and multi-solitons states. For example, with a peak power of 600 W, the hyperbolic secant trigger can generate 3-solitons, but the Gaussian and super Gaussian triggers cannot generate any cavity soliton. When the peak power increases to 750 W, the hyperbolic secant and Gaussian triggers generate 3- and 1-soliton state, respectively, but the super Gaussian trigger still cannot generate any cavity soliton. However, when the trigger peak power increases to 850 W, the hyperbolic secant, super Gaussian, and Gaussian triggers generate the 5-, 3-, and 1-soliton state, respectively. Thus, there is no obvious pattern on the impact of different profiles in multi-solitons transitions.

#### 4.4 Thermally self-stabilized cavity solitons

In comparison to large volume fiber and spatial cavities, thermal effects become much stronger in nano-scaled microcavities [46]. The dissipated energy heats up the cavities and induces the changing of the refractive indices. Thus, the resonant frequencies of the cavities will be shifted by the thermal effects and the pump-resonance detuning cannot be modeled as a fixed value any more. As discussed in Figure 6(b), for a given pump power, there is a region of pump-resonance detuning that cavity solitons (CSs) can be excited. But the thermal shift may push the detuning outside this region and thus disable the CSs excitation. The development of athermal optical materials and advanced cooling techniques are promising to overcome the thermal problem, but up to now, the techniques still cannot meet the requirements [47].

We include the thermal dynamics into the model and divide the temporal triggering procedure of the SCS states into two stages, i.e. the CW and CS stages. In the CW stage, only the CW pump accumulates in the cavity and reaches the thermally stabilized state. The resonant frequency will be correspondingly red-shifted towards the pump frequency, thus the pump-resonance detuning will be decreased. Then, in the CS state, the single shot trigger pulse is injected into the cavity with the CW pump to excite the SCS state. If the thermally changed pump-resonance detuning at the end of the CW stage still locates in the detuning region that supports CSs, the SCS can be excited by the trigger pulse in the early CS stage. In the process of the SCS excitation, the thermal dynamics will not prevent it since the thermal response time of  $\text{Si}_3\text{N}_4$  waveguide is much longer than the excitation time of CS and the thermally changed detuning is still very small in such transient time. As can be seen in Figure 7(a), the SCS excitation time is  $\sim 4$  ns (1000 roundtrips). In contrast, the thermal response time of  $\text{Si}_3\text{N}_4$  waveguide is at the order of microseconds or sub-microseconds [48,49]. However, the increase of intracavity energy induced by the pulse trigger can further shift the cavity resonant frequency, which might annihilate the SCS excited.

We first study the thermal effects in the CW stage. Since the intracavity CW field does not vary significantly between consecutive roundtrips and considering the extremely long thermal stabilization process, we use a modified LLE to improve the computation efficiency,

$$t_R \frac{\partial \psi}{\partial t} = \sqrt{\theta} \psi_{\text{in}} - \frac{\alpha_0 L + \theta}{2} \psi - i(\delta_0 + \delta_{\text{therm}}) \psi + iL \sum_{k \geq 2} \frac{\beta_k}{k!} \left(i \frac{\partial}{\partial \tau}\right)^k \psi + i\gamma L (1 + i\tau_{\text{shock}} \frac{\partial}{\partial \tau}) |\psi|^2 \psi, \quad (5)$$

$$\frac{d\delta_{\text{therm}}}{dt} = -\frac{\delta_{\text{therm}}}{\tau_0} + \frac{\xi}{t_R} \int_0^{t_R} |\psi|^2 dt, \quad (6)$$

where  $\delta_{\text{therm}} = t_R(\omega_{\text{therm}} - \omega_0)$  is the thermally induced detuning shift,  $\omega_{\text{therm}}$  is the thermal shifted cavity

resonant frequency.  $\tau_0$  is thermal response time determined by the material of microresonator and the thermal dissipation in experiments.  $\xi$  is the coefficient representing the detuning shift in response to the average intracavity power. We use  $\tau_0 = 100$  ns and  $\xi = -4.5 \times 10^4 \text{ W}^{-1} \text{ s}^{-1}$  in the simulation according to a practically fabricated high-Q ( $\sim 1.1 \times 10^6$ )  $\text{Si}_3\text{N}_4$  microresonator [49,50], which has the comparable volume and parameters to the one illustrated in Figure 1 except a smaller propagation loss of  $\alpha_0 L = 0.0012$ . Comparing to the thermal optics effect of  $\text{Si}_3\text{N}_4$ , the contribution of thermal expansion effect is much smaller and negligible [48,49]. Hence,  $\xi \propto \mathcal{R} \alpha_0 L$  depends on the thermal optic coefficient  $\mathcal{R}$  of  $\text{Si}_3\text{N}_4$ , the heat capacity  $C$  of the microring and the ratio that intracavity power is absorbed and converted to heat. We can use the  $\xi$  value at  $\alpha_0 L = 0.0012$  as a reference to calculate  $\xi$  at other loss parameters.

Figure 11(a) shows the stabilized  $\delta_1 \equiv \delta_0 + \delta_{\text{therm}}$  at the end of CW stage as a function of initial detuning  $\delta_0$  under different propagation loss and pump power. Simulations of Equations (5) and (6) in  $5 \times 10^6$  roundtrips time ( $\sim 22 \mu\text{s}$ ) are done to guarantee the thermal stabilization in the CW stage. We find that, for a given pump power and loss, there is a lowest initial detuning  $\delta_{0,\text{min}}$  to hold the detuning in red-shift side. Only with a  $\delta_0 \geq \delta_{0,\text{min}}$ , the final  $\delta_1$  can be positive, which is a necessary condition for CS excitation. When  $\delta_0 < \delta_{0,\text{min}}$ ,  $\delta_1$  will become negative (blue-detuning), thus no CS can be excited. With the increasing of propagation loss, the threshold  $\delta_{0,\text{min}}$  will also increase since more intracavity power is converted to heat. On another side,  $\delta_{0,\text{min}}$  will also increase if the pump power  $P_{\text{cw}}$  is increased.

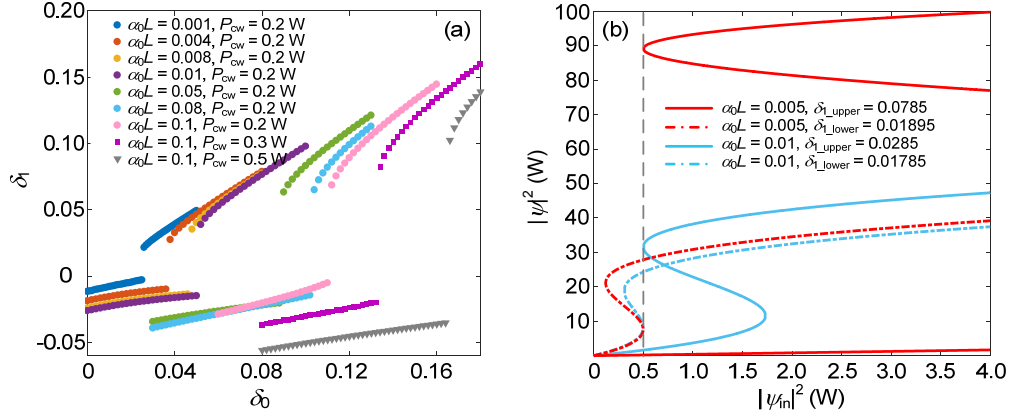


Figure 11 (a) Stabilized  $\delta_1$  at the end of CW stage as a function of initial detuning  $\delta_0$  under different propagation loss and pump power. Other parameters:  $\gamma = 1.4 \text{ W}^{-1}/\text{m}$ ,  $L = 628 \mu\text{m}$ ,  $\theta = 0.0025$ ,  $t_{\text{R}} = 4.425$  ps. (b) S-curves with the border detuning values  $\delta_{1,\text{lower}}$  and  $\delta_{1,\text{upper}}$  for the pump power of 0.5 W when  $\alpha_0 L$  are 0.005 and 0.01, respectively.

It is known that the CS states exist almost in the same bistable region of the stationary CW solution of the Ikeda map or the LLE [16,35,41]. The two models give the same bistability region as long as the nonlinear length scale is much longer than the cavity length [17,41]. Since the thermal effect responds in a long time scale, we can focus on the initial stage of the CS stage and obtain the stationary CW solution by setting the derivative terms in Equation (5) to zeros and neglecting the variation of  $\delta_1$  in the transient triggering process,

$$Y = \frac{\gamma^2 L^2}{\theta} X^3 - \frac{2\delta_1 \gamma L}{\theta} X^2 + \frac{(\delta_1^2 + \alpha^2)}{\theta} X, \quad (7)$$

where  $Y = |\psi_{\text{in}}|^2$  is the pump power,  $X = |\psi|^2$  is the intracavity power,  $\alpha = (\alpha_0 L + \theta)/2$  is the

variable substitution of loss. The turning points of the curve  $Y(X)$  can be found by setting the derivative  $dY/dX$  to zero as,

$$3\gamma^2 L^2 X^2 - 4\delta_1 \gamma L X + (\delta_1^2 + \alpha^2) = 0, \quad (8)$$

The curve  $X(Y)$  governed by Equation (7) has a bistable region when Equation (8) has two different real roots of  $X$ , which requires  $\delta_1^2 > 3\alpha^2$ . The two real roots corresponding to the two turning points of the bistable curve are given by,

$$X_{1,2} = \frac{2\delta_1 \pm \sqrt{\delta_1^2 - 3\alpha^2}}{3\gamma L}, \quad (9)$$

Substituting the roots into Equation (7), we can obtain the minimum and maximum  $P_{cw}$  in the bistable region with given  $\delta_1$  and  $\alpha$ . By sweeping  $\delta_1$ , the limited bistable regions can be found in the 2-dimensional space  $(P_{cw}, \delta_1)$ . The bistable regions in the  $(P_{cw}, \delta_1)$  space, with  $\alpha_0 L$  values varying ten times from 0.0012 to 0.012, are shown in Figure 12 as the green regions defined by the two border curves in each map. The two specific losses, i.e.  $\alpha_0 L = 0.0012$  and 0.012, correspond to two practically fabricated  $\text{Si}_3\text{N}_4$  microresonators [18,49,50]. The other two losses of  $\alpha_0 L = 0.004$  and 0.008 are randomly chosen between the two specific ones. In the green bistable region, there are two boundary detuning values  $\delta_{1\_upper}$  and  $\delta_{1\_lower}$  of  $\delta_1$  for each  $P_{cw}$  within the  $(P_{cw}, \delta_1)$  space. In the detuning range of  $\delta_{1\_lower} < \delta_1 < \delta_{1\_upper}$  with a given pump power  $P_{cw}$ , the system always has the bistable solution. Figure 11(b) shows two sets of the S-curves with the border detuning values  $\delta_{1\_lower}$  and  $\delta_{1\_upper}$  for a pump power  $P_{cw} = 0.5$  W. When the loss  $\alpha_0 L$  is 0.005, the  $\delta_{1\_upper}$  (red solid line) and  $\delta_{1\_lower}$  (red dashed line) are calculated to be 0.0785 and 0.01895, respectively. The difference between  $\delta_{1\_upper}$  and  $\delta_{1\_lower}$  is 0.0595. When  $\alpha_0 L$  is increased to 0.01,  $\delta_{1\_upper} = 0.0285$  (blue solid line) and  $\delta_{1\_lower} = 0.01785$  (blue dashed line) are obtained. Comparing to the case of  $\alpha_0 L = 0.005$ , the difference between  $\delta_{1\_upper}$  and  $\delta_{1\_lower}$  reduces to 0.0107, which means the range of valid  $\delta_1$  becomes narrower. The variation trend is accordant to that of the green regions in Figure 12.

If the thermally-stabilized detuning  $\delta_1$  falls into the region bounded by  $\delta_{1\_upper}$  and  $\delta_{1\_lower}$  at the end of the CW stage, SCS can be excited in a short period after the injection of the single shot trigger pulse. Figure 12 shows the calculated minimum  $\delta_1$  that can be stabilized in the red-detuning side by the blue dots and their fitting curves by blue dashed curves. In experiments, any combination of  $P_{cw}$  and  $\delta_1$  above the blue curves can be obtained by a properly chosen initial detuning  $\delta_0$  with assistance of the relation shown in Figure 11(a). Then we can easily find the valid regions (hatched regions in Figure 12) of SCS excitation under thermal effect, which are the overlapping regions of the green regions and the valid  $\delta_1$  regions. When the loss  $\alpha_0 L$  is increased, i.e. the Q-factor of the microresonator is decreased, Figures 12(a)-12(d) show that the region bounded by  $\delta_{1\_upper}$  and  $\delta_{1\_lower}$  becomes narrower. Meanwhile, the minimum pump power  $P_{cw}$  and detuning  $\delta_1$  in the hatched region are both increased. Since injecting a CW light with several watts power into the nanoscale waveguide is not practical, it is hard to excite the SCS in low-Q  $\text{Si}_3\text{N}_4$  microresonators under the influence of thermal effect. The threshold of the Q-factor to be defined as “low-Q” depends on the operation range of pump power. For the given pump power ranging from 0 to 1.2 W, Figure 12(d) shows that there is no valid region at  $\alpha_0 L = 0.012$  (Q-factor  $\sim 1 \times 10^5$ ). In contrast, when  $\alpha_0 L$  is 0.0012 (Q-factor  $\sim 1.1 \times 10^6$ ), Figure 12(a) shows the hatched region is quite large, which means the selection of initial  $\delta_0$  becomes more flexible.

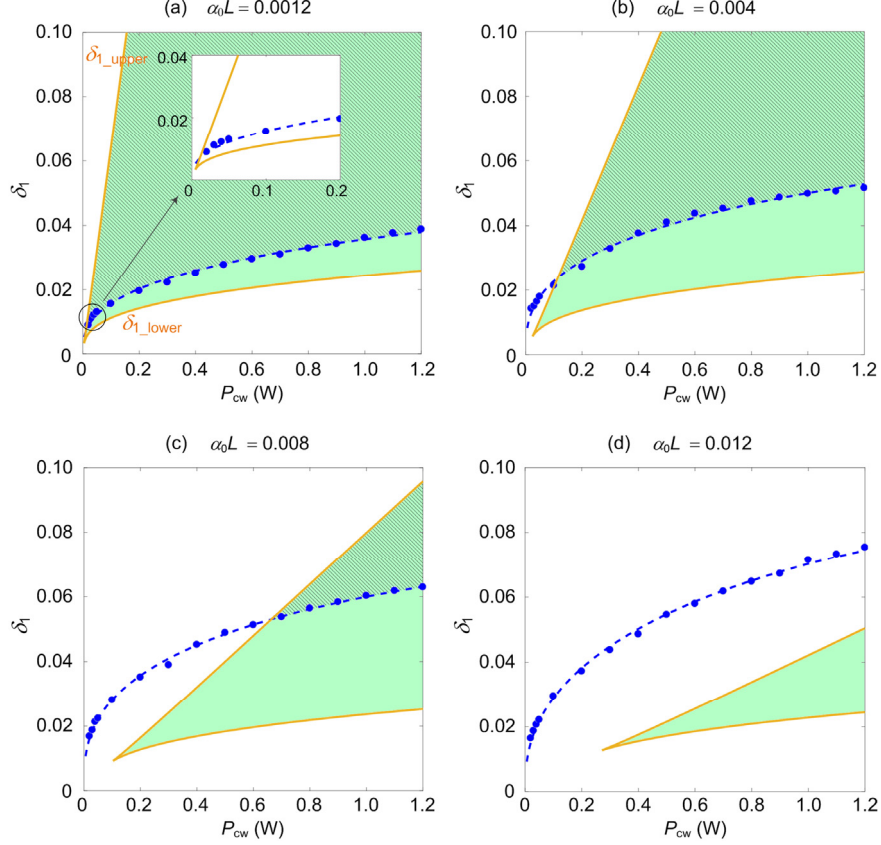


Figure 12 The green regions are the possible CS excitation regions (bistable regions) bounded by the detunings  $\delta_{1\_upper}$  and  $\delta_{1\_lower}$ . The blue dashed curves with dots show the minimum thermally stabilized  $\delta_1$  that can maintain in the red-shift side. The hatched regions indicate the valid regions for SCS excitation with the pulse trigger scheme. The loss  $\alpha_0 L$  is (a) 0.0012, (b) 0.004, (c) 0.008, and (d) 0.012, respectively. The inset in (a) shows the zoom-in view of the pump power ranging from 0 to 0.2 W.

In Figure 12(a), we randomly choose a combination of pump power  $P_{cw} = 0.03$  W and initial detuning  $\delta_0 = 0.018$  that supporting  $\delta_1$  to fall into the hatched region as an example, and simulate both the CW and CS stages with the thermal optics effect included. Considering both the coherent stacking of pulse trials of the leaked pulsed trigger and the fast variation of the intracavity field between consecutive roundtrips, we simulate the SCS triggering process in the CS stage using a modified Ikeda map, which is similar to the Equations (1) and (2) except changing  $\delta_0$  to  $\delta_0 + \delta_{therm}$  and adding the thermal dynamics governed by Equation (6). We also assume that the variation of  $\delta_{therm}$  is small in one roundtrip and update  $\delta_{therm}$  with a step of  $t_R$ .

Figures 13(a) and 13(b) show the temporal and spectral evolutions in along with the instantaneous temporal and spectral profiles at the end of the CS stage, respectively. The corresponding variations of intracavity average power and  $\delta_0 + \delta_{therm}$  are shown in Figures 13(c) and 13(d), respectively. The intracavity average power experiences a relaxation oscillation in the initial several hundreds of roundtrips (inset I of Figure 13(c)), then increases slowly in the long thermal stabilization process and eventually stops at a fixed power of 0.2772 W. The detuning  $\delta_0 + \delta_{therm}$  varies significantly in the first  $1 \times 10^6$  roundtrips of the CW stage and slowly converges to 0.016753 at the end. The thermal stabilization takes about  $2 \times 10^6$  roundtrips. The average power and the thermally induced detuning shift  $\delta_{therm}$  satisfy the stationary solution of Equation (6). A single 0.5 ps hyperbolic secant pulse with a peak

power of 7500 W is injected at the beginning of the CS stage. The SCS is excited in  $\sim 1000$  roundtrips (4.42 ns), and more attractively, survives and is thermally self-stabilized in the subsequent evolution. The average power and  $\delta_0 + \delta_{\text{therm}}$  are stabilized to 0.90375 W and 0.013933, respectively, in  $\sim 6 \times 10^5$  roundtrips of the CS stage. We believe the survival of the SCS under thermal perturbation benefits from the proposed pulse trigger approach. Unlike the frequency tuning method, in which the tuning process is typically microseconds level (comparable to or even longer than thermal response time) and the intracavity field experiences chaotic states to provide quite a lot of energy that converted to heat, the SCS can be directly excited in several nanoseconds without any chaotic dynamics under the proposed trigger approach. Hence, the thermal perturbation is very small in the short period excitation process because of the fast excitation and slow heating up. We find that the final detuning  $\delta_0 + \delta_{\text{therm}} = 0.013933$  is still in the green region and larger than the boundary value  $\delta_{1\_lower} = 0.0073$ . Thus, the SCS will not be annihilated but slowly adjust the CS working point with respect to the gradually changed detuning by thermal effect, finally is thermally self-stabilized. It should be pointed out that it is not recommended to excite the SCS with  $\delta_1$  close to the lower boundary  $\delta_{1\_lower}$ , where breather CS states may appear [51,52]. The energy of the breather CSs is continually changing so that it is hard to be thermally self-stabilization. The exact thermally self-stabilization region of the SCS is not given in this paper, which will be studied in future work. However, it is predictable that this region will become broader for high-Q microresonators since the energy converted to heat is less, and the CSs valid region bounded by  $\delta_{1\_upper}$  and  $\delta_{1\_lower}$  becomes broader.

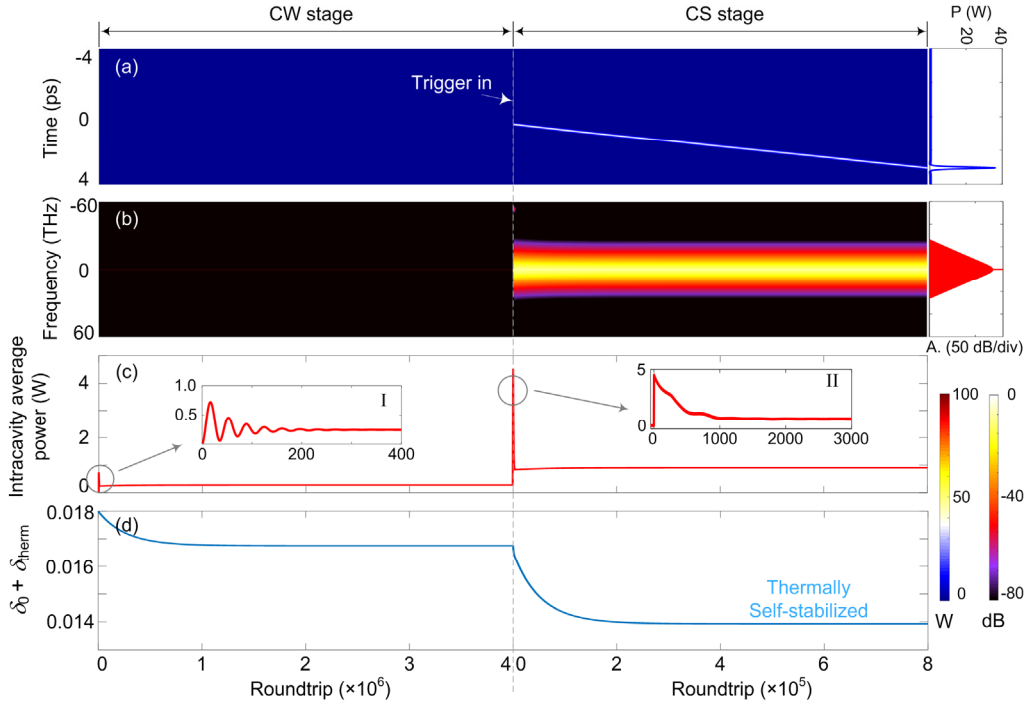


Figure 13 (a) Temporal evolution and final instantaneous temporal profiles (b) spectral evolution and final instantaneous spectral profiles in the CW and CS stages. (c) Evolution of intracavity average power. Inset I and II show the zoom-in views in  $[0, 400]$  roundtrips of CW stage and  $[0, 3000]$  roundtrips of CS stage, respectively. (d) Evolution of  $\delta_0 + \delta_{\text{therm}}$ .

## 5. CONCLUSION

In summary, we propose to directly and deterministically generate single-soliton Kerr comb in

microring resonator by seeding the CW pump field with a pulsed trigger. With properly selected pump frequency and pump-resonance detuning, single cavity soliton can be straightforwardly obtained without experiencing any multi-stable or chaotic states in the nonlinear cavity. Both low repetition rate pulse train and single shot pulse triggers with sufficient energy can be used to excite the desired SCS. The feasibility of single shot trigger approach makes it possible to manipulate the number of solitons and their temporal locations inside the cavity by simply controlling the power and temporal location of the single pulse trigger. The proposed trigger approach can be universally applied in different type of microresonators as long as the microresonators do support CSs. Moreover, we find that even under strong thermal effects the proposed trigger approach is valid in practically fabricated  $\text{Si}_3\text{N}_4$  microresonators. No additional complex engineering is required. Benefiting from the fast triggering process and the relatively small changing of intracavity energy, SCSs can be easily excited within a broad parameters range and thermally self-stabilized in long term evolution. Since the triggering process is insensitive to the detuning of the single shot trigger source when the trigger width is shorter to a certain degree than the roundtrip time, the choice of trigger source is very flexible and feasible. The finding of thermally self-stabilized SCSs confirms the feasibility of the proposed trigger approach to be immediately applied in the microresonators fabricated by current fabrication foundries to generate deterministic SCS. The proposed trigger approach contributes a direct and simple way to excite the desired SCS in monolithic microresonators, which will pave the way to the applications of single-soliton Kerr combs.

#### ACKNOWLEDGEMENT

This work is partly supported by the Research Grant Council of the Hong Kong Special Administrative Region China (PolyU152471/16E), The Hong Kong Polytechnic University (1-ZVGB), the National Natural Science Foundation of China (61307109, 61475023, and 61475131), the Beijing Youth Top-notch Talent Support Program (2015000026833ZK08), and the Shenzhen Science and Technology Innovation Commission (JCYJ20160331141313917).

<sup>†</sup>These authors contributed equally to this work.

#### REFERENCES

- [1] D. J. Jones, S. A. Diddams, J. K. Ranka, A. Stentz, R. S. Windeler, J. L. Hall, and S. T. Cundiff, *Science* **288**, 635 (2000).
- [2] S. T. Cundiff and J. Ye, *Reviews of Modern Physics* **75**, 325 (2003).
- [3] A. Schliesser, N. Picqué, and T. W. Hänsch, *Nature Photonics* **6**, 440 (2012).
- [4] J. Pfeifle *et al.*, *Nature Photonics* **8**, 375 (2014).
- [5] P. Del’Haye, A. Schliesser, O. Arcizet, T. Wilken, R. Holzwarth, and T. Kippenberg, *Nature* **450**, 1214 (2007).
- [6] T. J. Kippenberg, R. Holzwarth, and S. Diddams, *Science* **332**, 555 (2011).
- [7] T. Herr, K. Hartinger, J. Riemensberger, C. Wang, E. Gavartin, R. Holzwarth, M. Gorodetsky, and T. Kippenberg, *Nature Photonics* **6**, 480 (2012).
- [8] S. B. Papp, K. Beha, P. Del’Haye, F. Quinlan, H. Lee, K. J. Vahala, and S. A. Diddams, *Optica* **1**, 10 (2014).
- [9] C. Y. Wang, T. Herr, P. Del’Haye, A. Schliesser, J. Hofer, R. Holzwarth, T. Hänsch, N. Picqué, and T. J. Kippenberg, *Nature Communications* **4**, 1345 (2013).
- [10] T. Kobatake, T. Kato, H. Itohe, Y. Nakagawa, and T. Tanabe, *IEEE Photonics Journal* **8**, 1 (2016).
- [11] D. J. Moss, R. Morandotti, A. L. Gaeta, and M. Lipson, *Nature Photonics* **7**, 597 (2013).
- [12] Y. Okawachi, K. Saha, J. S. Levy, Y. H. Wen, M. Lipson, and A. L. Gaeta, *Optics Letters* **36**, 3398 (2011).

- [13] I. Barashenkov and Y. S. Smirnov, *Physical Review E* **54**, 5707 (1996).
- [14] T. Herr, V. Brasch, J. Jost, C. Wang, N. Kondratiev, M. Gorodetsky, and T. Kippenberg, *Nature Photonics* **8**, 145 (2014).
- [15] Y. K. Chembo and C. R. Menyuk, *Physical Review A* **87**, 053852 (2013).
- [16] S. Coen and M. Erkintalo, *Optics Letters* **38**, 1790 (2013).
- [17] S. Coen, H. G. Randle, T. Sylvestre, and M. Erkintalo, *Optics Letters* **38**, 37 (2013).
- [18] M. R. Lamont, Y. Okawachi, and A. L. Gaeta, *Optics Letters* **38**, 3478 (2013).
- [19] X. Xue, Y. Xuan, Y. Liu, P.-H. Wang, S. Chen, J. Wang, D. E. Leaird, M. Qi, and A. M. Weiner, *Nature Photonics* **9**, 594 (2015).
- [20] M. Erkintalo and S. Coen, *Optics Letters* **39**, 283 (2014).
- [21] H. Guo *et al.*, *Nature Physics* (2016).
- [22] M. Karpov *et al.*, in *CLEO: QELS\_Fundamental Science* (Optical Society of America, 2016), p. FM2A. 2.
- [23] X. Yi, Q.-F. Yang, K. Y. Yang, M.-G. Suh, and K. Vahala, *Optica* **2**, 1078 (2015).
- [24] V. Brasch, M. Geiselmann, T. Herr, G. Lihachev, M. Pfeiffer, M. Gorodetsky, and T. Kippenberg, *Science* **351**, 357 (2016).
- [25] J. A. Jaramillo-Villegas, X. Xue, P.-H. Wang, D. E. Leaird, and A. M. Weiner, *Optics Express* **23**, 9618 (2015).
- [26] C. Joshi, J. K. Jang, K. Luke, X. Ji, S. A. Miller, A. Klenner, Y. Okawachi, M. Lipson, and A. L. Gaeta, *Optics Letters* **41**, 2565 (2016).
- [27] M. Yu, Y. Okawachi, A. G. Griffith, M. Lipson, and A. L. Gaeta, *Optica* **3**, 854 (2016).
- [28] G. S. McDonald and W. J. Firth, *J Opt Soc Am B* **10**, 1081 (1993).
- [29] C. McIntyre, A. Yao, G.-L. Oppo, F. Prati, and G. Tissoni, *Physical Review A* **81**, 013838 (2010).
- [30] J. K. Jang, M. Erkintalo, S. Coen, and S. G. Murdoch, *Nature Communications* **6** (2015).
- [31] H. Taheri, A. A. Eftekhar, K. Wiesenfeld, and A. Adibi, *IEEE Photonics Journal* **7**, 1 (2015).
- [32] J. K. Jang, M. Erkintalo, S. G. Murdoch, and S. Coen, *Optics Letters* **40**, 4755 (2015).
- [33] W. Firth and A. Scroggie, *Physical Review Letters* **76**, 1623 (1996).
- [34] S. Barland *et al.*, *Nature* **419**, 699 (2002).
- [35] F. Leo, S. Coen, P. Kockaert, S.-P. Gorza, P. Emplit, and M. Haelterman, *Nature Photonics* **4**, 471 (2010).
- [36] J. K. Jang, M. Erkintalo, S. G. Murdoch, and S. Coen, *Nature Photonics* **7**, 657 (2013).
- [37] F. Leo, L. Gelens, P. Emplit, M. Haelterman, and S. Coen, *Optics Express* **21**, 9180 (2013).
- [38] M. Haelterman, S. Trillo, and S. Wabnitz, *Optics Communications* **91**, 401 (1992).
- [39] F. Li, J. H. Yuan, Z. Kang, Q. Li, and P. K. A. Wai, *Nanophotonics* **5**, 292 (2016).
- [40] T. Hansson, D. Modotto, and S. Wabnitz, *Optics Letters* **39**, 6747 (2014).
- [41] T. Hansson and S. Wabnitz, *J Opt Soc Am B* **32**, 1259 (2015).
- [42] M. Karpov, H. Guo, A. Kordts, V. Brasch, M. H. Pfeiffer, M. Zervas, M. Geiselmann, and T. J. Kippenberg, *Physical Review Letters* **116**, 103902 (2016).
- [43] C. Bao, L. Zhang, L. C. Kimerling, J. Michel, and C. Yang, *Optics Express* **23**, 18665 (2015).
- [44] Q. Lin, O. J. Painter, and G. P. Agrawal, *Optics Express* **15**, 16604 (2007).
- [45] Z. Wang, H. Liu, N. Huang, Q. Sun, J. Wen, and X. Li, *Optics Express* **21**, 1840 (2013).
- [46] T. Carmon, L. Yang, and K. J. Vahala, *Optics Express* **12**, 4742 (2004).
- [47] K. Padmaraju and K. Bergman, *Nanophotonics* **3**, 269 (2014).
- [48] X. Xue, Y. Xuan, C. Wang, P.-H. Wang, Y. Liu, B. Niu, D. E. Leaird, M. Qi, and A. M. Weiner, *Optics express* **24**, 687 (2016).
- [49] C. Bao, Y. Xuan, J. A. Jaramillo-Villegas, D. E. Leaird, M. H. Qi, and A. M. Weiner, *Optics Letters* **42**, 13

(2017).

[50] C. Bao, A. Weiner, Y. Xuan, D. Leaird, and M. Qi, in *CLEO: Science and Innovations* (Optical Society of America, 2017), p. SM2I. 1.

[51] C. Bao, J. A. Jaramillo-Villegas, Y. Xuan, D. E. Leaird, M. Qi, and A. M. Weiner, *Physical Review Letters* **117**, 163901 (2016).

[52] M. Yu, J. K. Jang, Y. Okawachi, A. G. Griffith, K. Luke, S. A. Miller, X. Ji, M. Lipson, and A. L. Gaeta, *Nature Communications* **8** (2017).